catalysts

MDPI

Article

Investigating Layered Topological Magnetic Materials as Efficient Electrocatalysts for the Hydrogen Evolution Reaction under High Current Densities

Sanju Gupta [1,2,3,*], Hanna Świątek [4], Mirosław Sawczak [5], Tomasz Klimczuk [4] and Robert Bogdanowicz [1,2]

[1] Department of Metrology and Optoelectronics, Faculty of Electronics, Telecommunication and Informatics, Gdansk University of Technology, Narutowicza Str. 11/12, 80-233 Gdansk, Poland; robbogda@pg.edu.pl
[2] Advanced Materials Center, Gdansk University of Technology, 80-233 Gdansk, Poland
[3] Department of Physics, Pennsylvania State University, University Park, PA 16802, USA
[4] Faculty of Applied Physics and Mathematics, Institute of Nanotechnology and Materials Engineering, Gdansk University of Technology, 80-233 Gdansk, Poland; hanna.swiatek@pg.edu.pl (H.Ś.); tomasz.klimczuk@pg.edu.pl (T.K.)
[5] The Szewalski Institute of Fluid-Flow Machinery, Polish Academy of Sciences, Fiszera 14, 80-231 Gdansk, Poland; mireks@imp.gda.pl
* Correspondence: sgup77@gmail.com or sangupta@pg.edu.pl

Abstract: Despite considerable progress, high-performing durable catalysts operating under large current densities (i.e., >1000 mA/cm^2) are still lacking. To discover platinum group metal-free (PGM-free) electrocatalysts for sustainable energy, our research involves investigating layered topological magnetic materials (semiconducting ferromagnets) as highly efficient electrocatalysts for the hydrogen evolution reaction under high current densities and establishes the novel relations between structure and electrochemical property mechanisms. The materials of interest include transition metal trihalides, i.e., $CrCl_3$, VCl_3, and VI_3, wherein a structural unit, the layered structure, is formed by Cr (or V) atoms sandwiched between two halides (Cl or I), forming a tri-layer. A few layers of quantum crystals were exfoliated (~50−60 nm), encapsulated with graphene, and electrocatalytic HER tests were conducted in acid (0.5M H_2SO_4) and alkaline (1M KOH) electrolytes. We find a reasonable HER activity evolved requiring overpotentials in a range of 30–50 mV under 10 mA cm^{-2} and 400−510 mV (0.5M H_2SO_4) and 280−500 mV (1M KOH) under −1000 mA cm^{-2}. Likewise, the Tafel slopes range from 27 to 36 mV dec^{-1} (Volmer–Tafel) and 110 to 190 mV dec^{-1} (Volmer–Herovsky), implying that these mechanisms work at low and high current densities, respectively. Weak interlayer coupling, spontaneous surface oxidation, the presence of a semi-oxide subsurface (e.g., O–$CrCl_3$), intrinsic Cl (or I) vacancy defects giving rise to in-gap states, electron redistribution (orbital hybridization) affecting the covalency, and sufficiently conductive support interaction lowering the charge transfer resistance endow the optimized adsorption/desorption strength of H* on active sites and favorable electrocatalytic properties. Such behavior is expedited for bi-/tri-layers while exemplifying the critical role of quantum nature electrocatalysts with defect sites for industrial-relevant conditions.

Keywords: quantum magnetic layered materials; HER; alkaline/acid electrolytes; overpotential; Tafel slope

check for updates

Citation: Gupta, S.; Świątek, H.; Sawczak, M.; Klimczuk, T.; Bogdanowicz, R. Investigating Layered Topological Magnetic Materials as Efficient Electrocatalysts for the Hydrogen Evolution Reaction under High Current Densities. *Catalysts* **2024**, *14*, 676. https://doi.org/10.3390/catal14100676

Academic Editor: Carlo Santoro

Received: 7 August 2024
Revised: 29 August 2024
Accepted: 4 September 2024
Published: 1 October 2024

1. Introduction

Catalytic and redox processes occurring on electrode surfaces are attracting enormous interest since they play a significant role in our lives and are ubiquitous in chemistry. For instance, the Haber–Bosch process is used to convert hydrogen and nitrogen into ammonia, which is a key ingredient for fertilizers to sustain the global food supply. Likewise, within the Sustainable Development Goals (SDG), the large-scale production and safe storage of hydrogen fuel is playing a pivotal role in energy transition strategies since hydrogen is one of the most efficient energy solutions. Electrocatalysis holds the key to enhancing the efficiency and cost-effectiveness of water-splitting devices, thereby contributing to the advancement of hydrogen as a clean sustainable energy carrier. The research and development of water splitting with Earth-abundant and cost-efficient electrocatalysts for large industrial level current density are vital for H_2 production. However, most of the reported catalysts are usually evaluated at small current densities (<100 mA cm^{-2}), far from satisfactory for industrial applications. Thus, searching for high-performance novel electrocatalysts for hydrogen evolution reactions (HER) is an important subject around PGM (platinum group metal)-free catalysis. Hydrogen (H_2) production through electrochemical water splitting has been considered a "green" and sustainable energy resource to fossil fuels by utilizing elemental Pt, Ni, semiconducting oxide TiO_2, and bi-metal (Fe-Ni, Pt-Pd, and Pt-Ir) catalysts [1–4]. Since the emergence of photocatalytic water splitting [5], HER has attracted enormous attention because it requires harvesting only water and is useful for fuel cells as the reverse reaction [6–8]. The possibilities for enhancing the catalytic activity in HERs are facilitated by traditional methods of increasing the concentration or areal density of active sites, metallicity by means of nanostructuring, doping, straining, and edge-plane sites, as well as enhancing the metal–oxide (Me-O) covalency. However, the reported electrocatalysts in the literature are often complex, irreproducible, and have uncertain exposed crystal facets/surfaces and a high density of defects, which can give rise to only an order of magnitude higher efficiency compared with catalysts of high intrinsic activity. Moreover, these efforts have a large reaction overpotential of 100–200 mV (ca. 382 mV for MoS_2 and 671 mV over commercial Pt/C), referred at a current density of 10 mA cm^{-2} and activation barriers significantly larger than the theoretical minimum of 1.23 V [9,10]. Despite rapid progress, materials' design and advancing their principles will have a significant impact on the knowledge to improve the performance of electrocatalysts for the forthcoming hydrogen economy. The current state-of-the art research in the development of electrocatalysts, highlighting the principal design rules inspired by solid-state materials chemistry and contributing to industrial applications, has been reported [11–14].

Two-dimensional (2D) layered transition metal dichalcogenides (TMDCs) have been widely investigated as prospective electrocatalysts for H_2 generation, particularly modulation with sulfur vacancy, edge-planes sites, phases, and isoelectronic (W and Se) doping, which have been demonstrated experimentally and supported with DFT calculations [9,10,15–17]. However, electron hopping across the layer is unfavored because of large interlayer potential barriers leading to occasional sluggish electron transfer and subsequent injection into the surface adsorbates [15]. Transition metal carbides (MXene) and oxides have emerged as major testing grounds for experimental and theoretical investigations into electrochemical properties and associated electronic structures and surface reconstructions [18]. As the closest 3D analog to 2D materials, the layered oxide perovskite Sr_2RuO_4 (SRO) attracted intense interest because of its *d* orbital electronic correlation-derived exotic properties (superconductivity, surface magnetism, and good metallicity) influencing catalysis applications [19,20]. However, research studies conducted on SRO's electrocatalytic properties was mostly conducted with polycrystalline samples and under a low current density range of ~10–100 mA cm^{-2} [21].

The emergent topological materials, a major category of quantum materials (topological insulators; TI, Dirac–Weyl semimetals, and nodal line semimetals), are at the forefront of improved technological performance, characterized by robust non-trivial topological surface states (TSSs) protected from lattice disorders attributed to band structure topology giving rise to favorable topological electronic bands [22,23]. Thus, quantum phenomena have mesmerized the scientific community, gaining increasing attention in physical and materials science for quantum information science, quantum sensing, and the unchartered territory of alternative energy for multi-junction photovoltaics as quantum catalytic electrodes, thereby going beyond the empirical development of electrocatalysts [24]. Moreover, the band inversion in these topological electronic phases surpasses local electroactive site optimization with the abovementioned robust TSSs, such that high conductivity (especially with defects) and carrier mobility can significantly influence interfacial charge transfer (R_{ct}) and ion transport behavior during complex electrocatalytic processes (e.g., multielectron, quantum tunneling) at the electrode/electrolyte interface [25,26]. Additionally, the protective surface states act as electron acceptors (*p*-type) or donors (*n*-type) for adsorbed molecules consequently tailoring the desired adsorption energy (ΔH_{ad}) and Gibbs free energy (ΔG_{ad}) induced by the topological quantum phase with a specific electronic structure [27]. As opposed to surface states or Shockley states, TSSs have a unique electronic structure that allows exploring quantum phenomena in surface chemistry such as that conducted in this work, thereby looking at (electro)catalysis through the lens of inventive quantum topology. Among various topological materials, Weyl semimetals: 1T′–$MoTe_2$, NbP, TaP, NbAs, NbS, and TaAs; topological insulators: Bi_2Se_3, Ti_2Te_3 and Sb_2Te_3, the triple-point metal MoP and the nodal line semimetal $PtSn_4$ have proven to be excellent catalysts for photoelectrochemical water splitting [23,25,28].

Among layered materials exhibiting quantum properties in bulk form down to the monolayer limit, the transition metal trihalides (MX_3, M = Cr, V; X = Cl, Br, I) play a central role; these are van der Waals ferromagnetic or antiferromagnetic materials exhibiting both insulating and semiconducting behavior [29,30]. It is interesting to note that few layers of these materials show a buckled honeycomb lattice—topologically equivalent to that of graphene—showing pseudo-relativistic massless Dirac Fermions, with possible multiple Dirac cones and spin texture due to strong spin-orbit coupling (SOC) useful for scattering free quasi-two-dimensional spintronics, also sought for catalysis due to the available conducting channels for fast electron and ion transportation. This work examines the electrocatalytic properties of multilayer $CrCl_3$, VCl_3, and VI_3 (and VI_2) as prime case-study systems. For a given structural unit $CrCl_3$ (and VCl_3, VI_3), where the Cr (or V) atom sits in a honeycomb planar lattice, the layered structure is formed by trilayers in which the Cr (or V) atoms are sandwiched between two halide layers [29,31]. In addition, some of the crystals (e.g., $CrCl_3$ and VI_3) appear to spontaneously oxidize upon air exposure (O–$CrCl_3$ and O–VI_3), limiting their placement on substrates; thus, attention was paid to encapsulation with a graphene equivalent (i.e., reduced graphene oxide, rGO, 5-nm-thick coating) required for the experiments to be viable. They were experimentally studied in a reduced dimension, exfoliated into larger multilayer flakes starting from bulk having a several micron lateral dimension and a few nanometers in thickness. We investigated the electrochemical HER response in alkaline (and acid) electrolytes, while they remained stable under high current densities, in addition to their complementary structural properties. The data collected were analyzed to determine the overpotential and Tafel slope, identifying the principle kinetic reaction mechanism (Volmer–Heyrovsky or Volmer–Tafel) and the TOF (turnover frequency). The high catalytic performance, with low overpotential (at high current densities), reasonable stability, and effective active site density, is attributed to the control of layers, the surface oxygenation (wettability), and the intrinsic Cl or I defect density, leading to in-gap states [32–34], which enable them to be potential quantum catalysts for further investigations with control of the layer number and deliberate oxygenation. These results are compared with continuous few-layer MoS_2, graphene/MoS_2 heterojunctions, SRO, commercial Pt/C, and others for accelerated discovery in durable electrocatalysts design [35–38].

2. Results and Discussion

This section describes the results and discussion related to the microscopy, crystal structure, and electrocatalytic properties of all MX_3 (along with VI_2) studied in this work. Figure 1 shows the optical images (panels a–d) and SEM micrographs (panels f–h) of the single crystal materials from which a few layers were exfoliated; nevertheless, they remained a bulk, since the thickness was ~50–60 nm, determined from the surface profilometer. The as-grown crystals show their characteristic intense hue in the form of shiny bright purple ($CrCl_3$), blackish (VCl_3 and VI_3), and red orange (VI_2) flakes, as shown in

Figure 1, and apparent lamellar or layer-like features in both sets of micrographs. The crystals were stored and manipulated in a glove box with an Ar (Argon) gas atmosphere to avoid oxidation and water contamination.

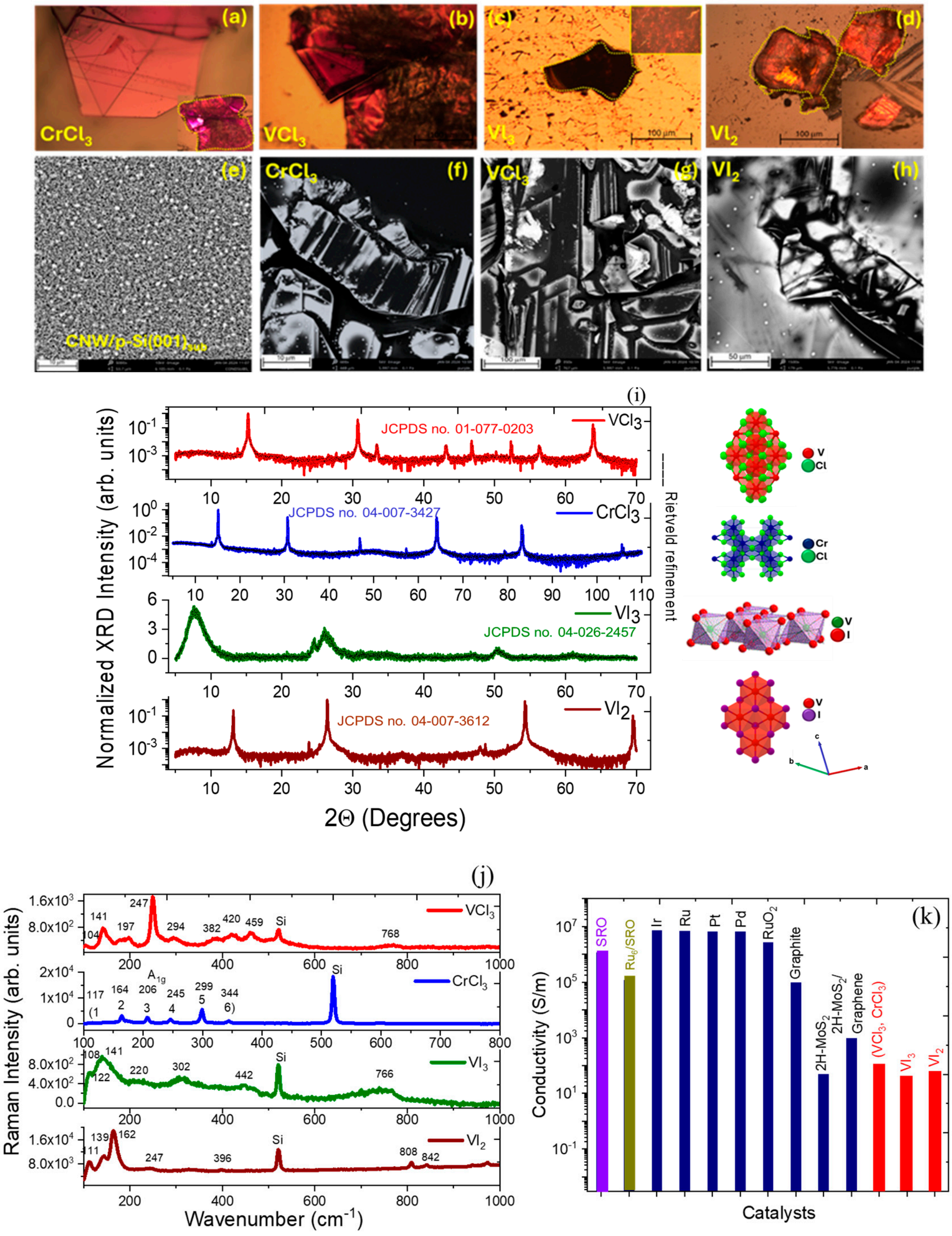

Figure 1. Morphology and structure. (**a**–**d**) Optical photographs; (**e**–**h**) scanning electron micrographs; (**i**) θ–2θ XRD patterns; (**j**) Micro-Raman spectra excited with 514 nm of few-layered $CrCl_3$, VCl_3, VI_3, and VI_2 crystals; and (**k**) room-temperature electrical conductivity comparison with other reported HER catalysts. Also provided are conventional unit cells of MX_3 crystals with their respective colored atoms, Rietveld refinement, JCPDS nos., and an SEM image of substrate CNW/p–Si (001).

Interestingly, the representative SEM images of cleavable VCl_3 and VI_2 crystals also show occasional white dots on their surface, which may be due to the aggregation of the material during vapor transport growth. The SEM image of the substrate is also provided (panel e). The energy dispersive spectroscopy (EDS) analysis was performed with SEM, corroborating the composition and stoichiometry of these crystals reported earlier in ref. [39]. The crystal structure is determined from the X-ray diffraction (XRD) along with Rietveld refinement and micro-Raman spectroscopy (RS) at room temperature, as they were mostly stable in the air for tens of hours, except for VI_3, which was marginally unstable but less pronounced than the reported CrI_3 crystals [30,40]. However, the microscopic images of a few flakes of all these crystals at the micron level upon air exposure showed no direct evidence of morphological degradation. This is because MX_3 has a semi-oxidized stable O–MX_3 surface phase that is stable up to 400 °C with charge imbalance, and this phase protects the inner pristine material [33,34]. Nevertheless, for reliable practical applications, the surface of the crystal layers was encapsulated with reduced graphene oxide for protection. Figure 1 (panels i and j) shows the representative XRD and Raman spectra of bulk crystals, respectively, displaying the characteristic peaks associated with their crystal/lattice structure. Since a flake-like single crystal was used for the XRD experiment, only (00l) reflections are observed. The as-synthesized $CrCl_3$ crystal adopts a monoclinic $C_{2/m}$ (No. 12) space group like the VI_3, where there are eight atoms in a primitive cell, while the VCl_3 and VI_2 crystallize in a two-dimensional trigonal $R\overline{3}$ (rhombohedral, No. 148) and $P\overline{3}m1$ (hexagonal, No. 163) space group, respectively, as shown in Figure 1i (right) [41–44]. The calculated lattice parameters (a) and crystallite size (L_{00l}) of these crystals from XRD, following Bragg's law and the Debye–Scherrer formula are $CrCl_3$: a = 6.02 Å, b = 6.02 Å, c = 17.87 Å, L_{hkl} = 0.308 Å; VCl_3: a = 6.06 Å, b = 6.06 Å, c = 6.94 Å, L_{hkl} = 0.325 Å; VI_3: a = 6.84 Å, b = 11.84 Å, c = 6.95 Å, L_{hkl} = 0.052 Å; and VI_2: a = 4.12 Å, b = 4.12 Å, c = 7.12 Å, L_{hkl} = 0.317 Å. The other values of the lattice parameters are reported from ref. [32,34]. The surface sensitive Raman spectrum of $CrCl_3$ shows resonant lattice vibrations at 116.9 cm^{-1}, 164.4 cm^{-1}, 206.5 cm^{-1}, 245.0 cm^{-1}, 300.0 cm^{-1}, and 345.0 cm^{-1}, typical of a few-layered crystal sample. The data are consistent with a recent report, where extensive work was carried out as a function of temperature and light polarization [45]. These resonances are assigned to A_g optical modes labeled as A_g (1–6), and the energy degenerates with B_g optical modes, according to the group theory and lattice dynamical calculations (i.e., $\Gamma_{optic} = 6A_g + 4A_u + 6B_g + 5B_u$) [46]. Likewise, the VCl_3 shows some resonance bands at 104 cm^{-1}, 141.2 cm^{-1}, 197.4 cm^{-1}, and 225.1 cm^{-1} (247 cm^{-1}) and a collection of three peaks between 380 and 460 cm^{-1}, in addition to a peak at 520.7 cm^{-1}, associated with the Si substrate detected in all spectra. For the VI_3 and VI_2 layers, the Raman spectra consisted of a few bands at 108.3 cm^{-1}, 122.5 cm^{-1}, 141 cm^{-1}, 220.1 cm^{-1}, 247.1 cm^{-1}, 302.1 cm^{-1}, 396.1 cm^{-1}, and 442.3 cm^{-1}, which is also in agreement with the literature [47–49]. All the Raman spectra were normalized with respect to the highest intensity Raman band for the respective spectra. Figure 1 (panel k) provides the room-temperature electrical conductivity comparison of the pristine MX_3 crystals' surface with other catalysts, and the values are taken from the sources cited in this work that are typical for semiconductors ($10-10^3$ S.m^{-1}) [50]. Meanwhile, the edge states' conductivity is anticipated to be larger and comparable to the conductivity of the most reported metal, metal-oxide, and sulfide electrocatalysts [19,47].

Having established the crystal structures and layered morphology, we now turn to the HER catalytic investigations. Prior to the performance assessment of the crystals' layers as a working electrode, the conductive support for its negligible HER activity contribution was evaluated. The electrocatalytic HER activity of metal trihalide quantum catalysts (alongside VI_2) were evaluated in 1.0 M KOH and 0.5 M H_2SO_4 electrolytes. As a reference, the HER performance of commercial Pt/C is also included under the same conditions. The hydrogen production activity was examined by the LSV polarization curves, depicted in Figure 2c,d, in addition to the cyclic voltammograms (CV) [Figure 2a,b] measured through a three-electrode electrochemical cell configuration in both acid and alkaline electrolytes.

To correct for the measured potentials due to solution resistance (R_S), they were subjected to *iR* correction in the LSV curves according to E = E_{RHE}-*iR*, where E is the *iR*-corrected potential, E_{RHE} is the measured potential with respect to RHE, *i* is the measured current, and *R* is the uncompensated resistance as determined from the *ac* EIS Nyquist plot for better accuracy (see Figure S1, Supplementary Information, also showing the Bode–Bode plot), rather than during the experiment. EIS data analysis through an equivalent Randles circuit (Figure S1 inset, Supporting Information) allows for the examination of electron transfer at the catalysts' surface/interface. The low charge transfer resistance (R_{ct}) of VCl_3 (and of others) in acidic (187.4 Ωcm^{-2}) and alkaline (200.2 Ωcm^{-2}) media regulates the electronic structure through interface interactions, thereby reducing the electron transfer (or ion transportation) resistance. Qualitatively, the cyclic voltammogram profiles appear asymmetric with broad peaks in both the electrolytes and the non-Faradaic region; these were analyzed to deduce the value of the electrochemical double-layer capacitance (C_{dl}) [Figure 2c]. The C_{dl} values of VCl_3 and VI_3 are 7.80 mF cm^{-2} and 8.80 mF cm^{-2}, respectively, which are higher than that of $CrCl_3$ (1.62 mF cm^{-2}) and VI_2 (0.80 mF cm^{-2}). Additionally, the electrochemically active surface area (ECSA) can be analyzed through the electrochemical double-layer capacitance (C_{dl}), and this was utilized to delve deeper into the HER kinetics in the catalysis process. Considering that these crystals have lower surface areas than the nanostructured catalysts, we are inclined to say that these crystals have topological protected surface states at j > 100 mA cm^{-2}.

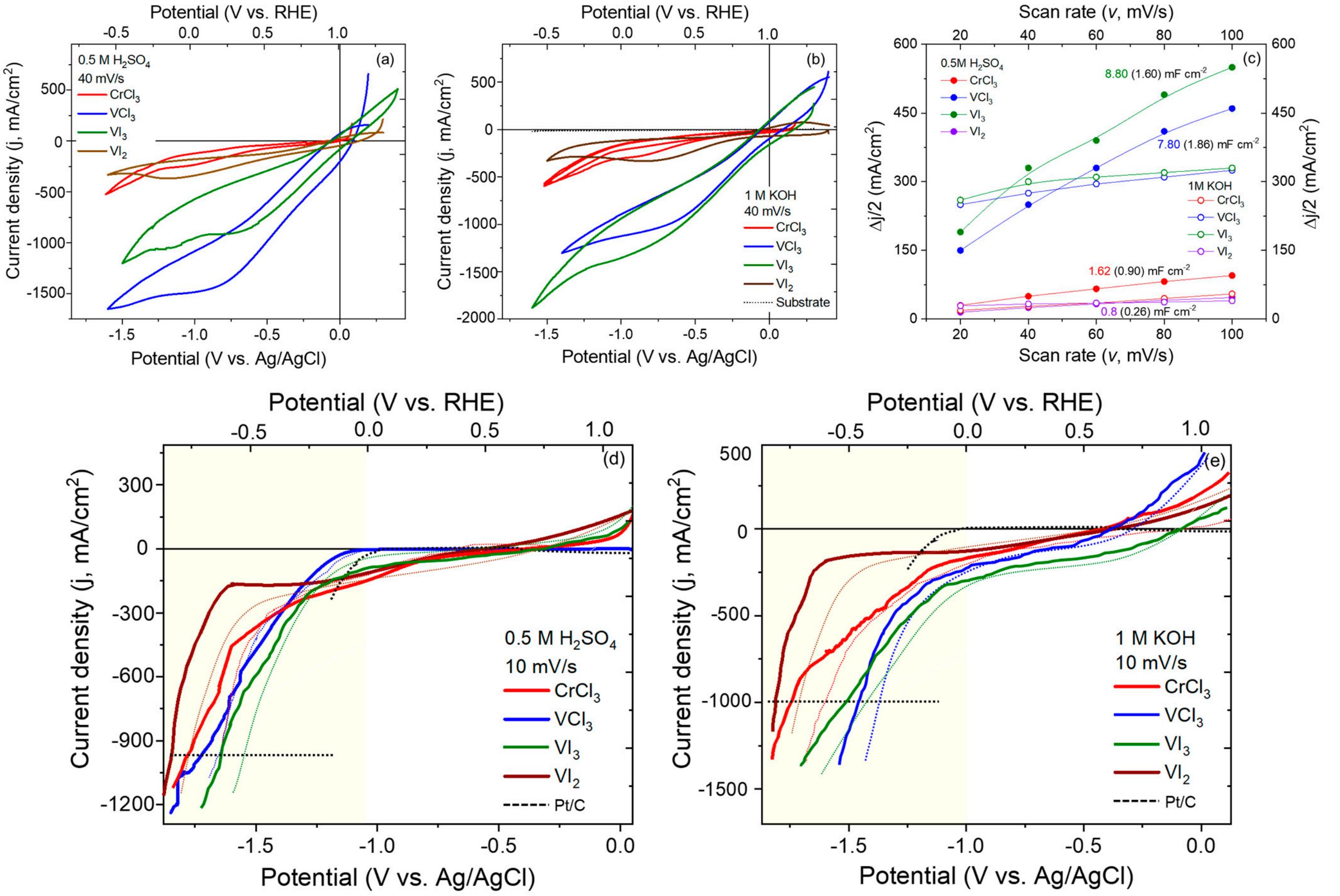

Figure 2. Cyclic voltammograms and HER polarization curves. (**a**,**b**) CV profiles, (**c**) capacitive current density difference versus scan rate, and (**d**,**e**) LSV polarization curves plotted in a large overpotential range with (dotted) and without (solid) considering *iR* ohmic drop of few-layer $CrCl_3$, VCl_3, VI_3, and VI_2 crystals, in acidic (0.5M H_2SO_4) and alkaline (1M KOH) electrolytes.

Interestingly, all the catalysts exhibited reasonable HER activity shown in the LSV curves (Figure 2d,e), although they tended to be broader compared to the Pt/C and MoS_2 where the hydrogen evolution profiles were sharper or change downward rapidly. The order of the electroactivity was VCl_3 (400 mV) > VI_3 (490 mV) > $CrCl_3$ (500 mV) > > VI_2 (515 mV) [VI_3 (270 mV) > VCl_3 (450 mV) > $CrCl_3$ (510 mV) > VI_2 (600 mV)], at a current density of 1000 mA cm^{-2} in acidic (alkaline) electrolytes, highlighting the significance of the quantum catalysts at an industrial scale, with Pt/C having the lowest overpotential of 62 mV in acidic and 101 mV in alkaline media, at 200 mA cm^{-2}. Interestingly, recent research reported for bimetallic sulfides evaluated for HER in an alkaline electrolyte required low overpotentials of 333 mV to reach 1000 mA cm^{-2} with long–term durability comparable to those found in this work for MX_3 quantum materials [11,14]. It is important to note that water splitting for commercial electrolyzers occurs at about 0.55 to 0.77 V higher than the theoretical value (ca. 1.23 V), an excess potential indispensable to overcome the energy barrier of the reaction system. The Tafel slope is employed to further assess the HER catalytic reaction kinetics, as shown in Figure 3a–c. The values of the Tafel slopes derived from the LSV curves (Figure 3a,b) ranged between 27 and 36 mV dec^{-1}, implying that they afford faster reaction kinetics during hydrogen production, comparable to Pt/C (ca. 20 and 39 mV dec^{-1}). Typically, electrochemical water splitting includes an oxygen precipitation reaction (oxygen evolution reaction, OER) and a hydrogen precipitation reaction (hydrogen evolution reaction, HER). It is widely accepted that the HER takes place on the surface of the cathode via a multi-step electrochemical reaction process [51,52]. Specifically, the kinetic reaction pathways in an acidic electrolyte occurs via the following reactions [53,54]: $H_3O^+ + e^- \ H_{ads} \rightarrow H_{ads} + H_2O$ (Volmer); $H_{ads} + H_3O^+ + e^- \rightarrow H_2 + H_2O$ (Herovsky); $2H_{ads} \rightarrow H_2$ (Tafel), and in an alkaline/neutral electrolyte, the kinetic steps involve the hydroxide ion: $2H_2O + 2e^- \rightarrow 2H_{ads} + 2OH^-$ (Volmer) and $2H_2O + 2e^- \rightarrow 2H_{ads} \rightarrow H_2 + 2OH^-$ (Herovsky); meanwhile, the Tafel step remains unchanged [55–58]. Thus, the Tafel slope is an important parameter to predict the HER mechanism, i.e., whether the HER process will proceed via the Volmer–Heyrovsky or Volmer–Tafel mechanism. Both the Tafel step and Heyrovsky step are related to the desorption of the hydrogen molecule from the electrocatalyst surface. The low Tafel slope (30–40 mV) in electrolytes suggests the rate-determining step for HER follows the Volmer–Tafel mechanism at low current densities, i.e., it should be the adsorbed hydrogens rather than the water dissociation determined for the MX_3 and VI_2 crystals, aided by the subsurface semi-oxide and unsaturated bonds induced by the edge vacancy/defects. Consequently, the HER reaction pathway at high current densities is governed by the Volmer–Herovsky mechanism. More importantly, by comparing the LSV curves and the Tafel slopes with those of commercial Pt/C under acidic and alkaline/neutral conditions, one can find that the alkaline HER performance of VI_3 is close to the acidic HER behavior of Pt/C, suggesting the acid-like HER behavior of VI_3 in an alkaline medium. In addition, the stability in 1 M KOH was implemented via a chronoamperometry test, and the current density of 100 mA cm^{-2} remained unchanged after several hours of operation.

It is also worth mentioning that the working mechanisms of HER catalysts under low and high current densities are significantly different, which is discussed below. Re-examining the Tafel slopes at a larger current range of 1000 mA cm^{-2}, the Tafel slopes determined for these electrocatalyst crystals layer ranged between 100 and 110 mV dec^{-1} and 185 and 200 mV dec^{-1} under acidic and alkaline electrolytes, respectively, implying that the recombination of adsorbed hydrogens is the rate-determination step. This means there are no electrons involved during the chemical reaction (Volmer–Tafel step). It is interesting to note that these values are comparable to those state-of-the-art Pt catalysts, with the Tafel slope as 125 mV dec^{-1} at 300 mA cm^{-2} in 0.5M H_2SO_4. However, the Tafel slope is potential dependent; thus, so too is the surface coverage of intermediate species (θ) [59]. The value is close to the prediction at the highest coverage $\theta = 1$, indicating the rapid hydrogen adsorption at large current densities. In addition, lower Tafel slopes guarantee low applied voltage during industrial-relevant conditions, as elucidated in

Figure 3c, providing discerning behavior for low and high current densities, as well as low and high overpotential corresponding to low and high surface coverage.

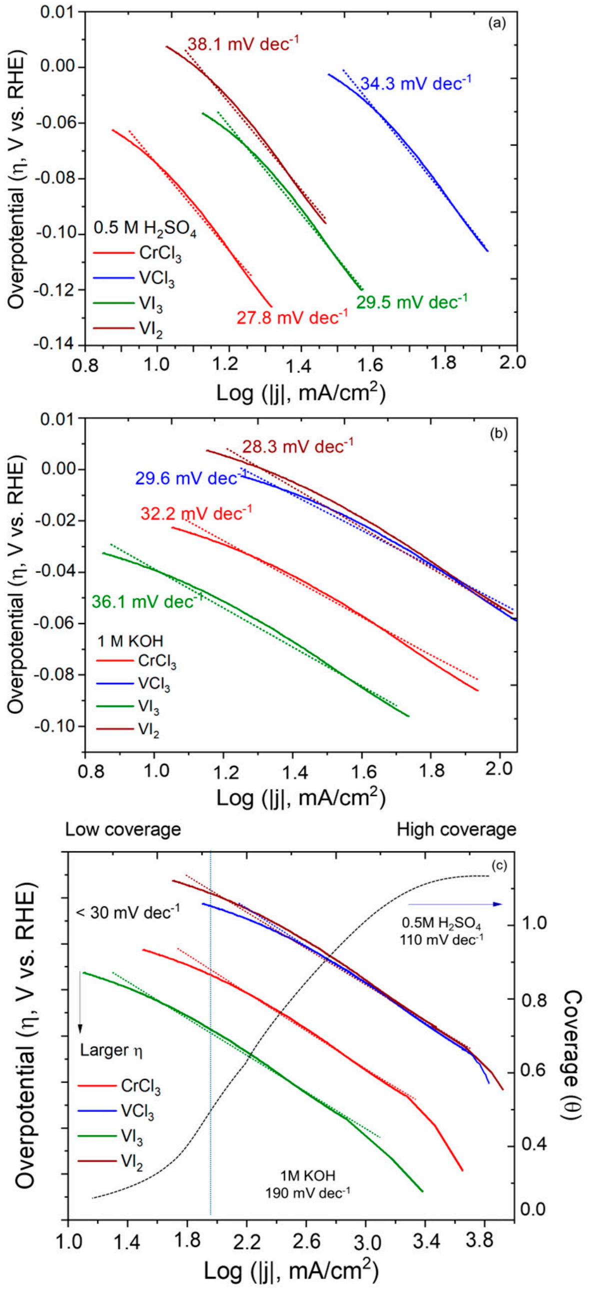

Figure 3. Overpotential and Tafel slopes under low and high current densities. Overpotential versus log current density, |j|, and Tafel slopes under low current densities of few-layer $CrCl_3$, VCl_3, VI_3, and VI_2, in (**a**) acidic (0.5M H_2SO_4) and (**b**) alkaline (1M KOH) electrolytes. (**c**) Corresponding Tafel slope analysis under high current densities. The dotted curve shows the coverage-dependent current densities.

At a fundamental level, the trends in catalytic activity are rationalized by the *d*-band theory, which assumes that metal–adsorbate interactions are characterized by the hybridization of the metal d–band with the bonding σ–orbital of the adsorbate, forming the basis of the electrocatalytic reactions following a volcano plot (i.e., log current density versus ΔG_{ads}). Thus, the catalytic reactions of layered topological magnetic materials should shift towards the metals with weak reactivity due to their TSSs (surface effect) and magnetic (bulk) character. In addition, they have shown good electron transport with reasonable conductivity due to the complex Fermi surface (see Figure 4). Figure 5 illustrates the experimental scheme (panel a) and the ingredients proposed to be responsible for the HER in relation to the atomic defects (panels b and c) in the two-dimensional view of crystals and (panel d) the electronic structure (DOS) of complex topological quantum electrocatalysts with the coexistence of the WSM (Weyl semimetal) and DNL (Dirac nodal line) behavior of the surface/edge states. Because of the time-reversal symmetry protection, the electrons stay longer on these materials surface states without dissipation that can populate the conduction band, such that they are readily supplied to H^+ ions for HER. Furthermore, the presence of multiple Dirac cones and band crossing leads to a large density of states, which can be another possibility as predicted by theory [60]. This can facilitate the rapid charge transfer associated with the catalytic process, thereby accelerating the HER kinetics. This performance for metal trihalides can be attributed to multivalent metal (V and Cr), the presence of intrinsic defects, and subsurface semi oxidation (O–MX_3), providing more (re)active sites and the delocalization of electrons leading to better HER activity [32]. The oxygen-containing species act as perfect ligands for surface engineering, considering these groups can form hydrogen bonding and attract hydronium ions/water reactant molecules to the surface. Therefore, a well-conditioned surface is required for desirable HER kinetic advancements. Therefore, modifying the electronic structure, which is defective and oxidized, as well as TSS, would be a more effective approach than the traditional method of creating only electroactive sites, thereby providing a guide in the search for high-performance electrocatalysts for HER. Finally, the HER reaction efficiency can be evaluated through H adsorption free energy (ΔG_H), and for a thermodynamically favorable HER process, a close to zero or small negative value is identified (see Figure S2, Supporting Information, for a comparison of the reported calculated values for HER catalyst surfaces with an anticipated estimate for defective/oxygenated MX_3, yet to be directly demonstrated). Our study provides strategic quantum materials for efficient PGM-free electrocatalysts for strategic industrially relevant clean energy-related applications within the SDGs.

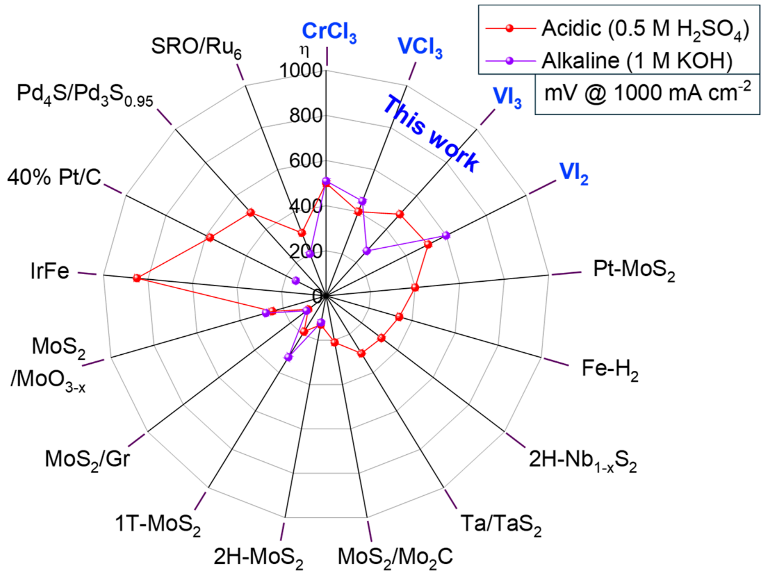

Figure 4. Performance evaluation. Comparison of the required overpotentials to reach the current density of 200 mA cm^{-2} and 1000 mA cm^{-2} between the recently reported catalysts to those studied here. The scale bar of the catalysts is based on the LSV measurements.

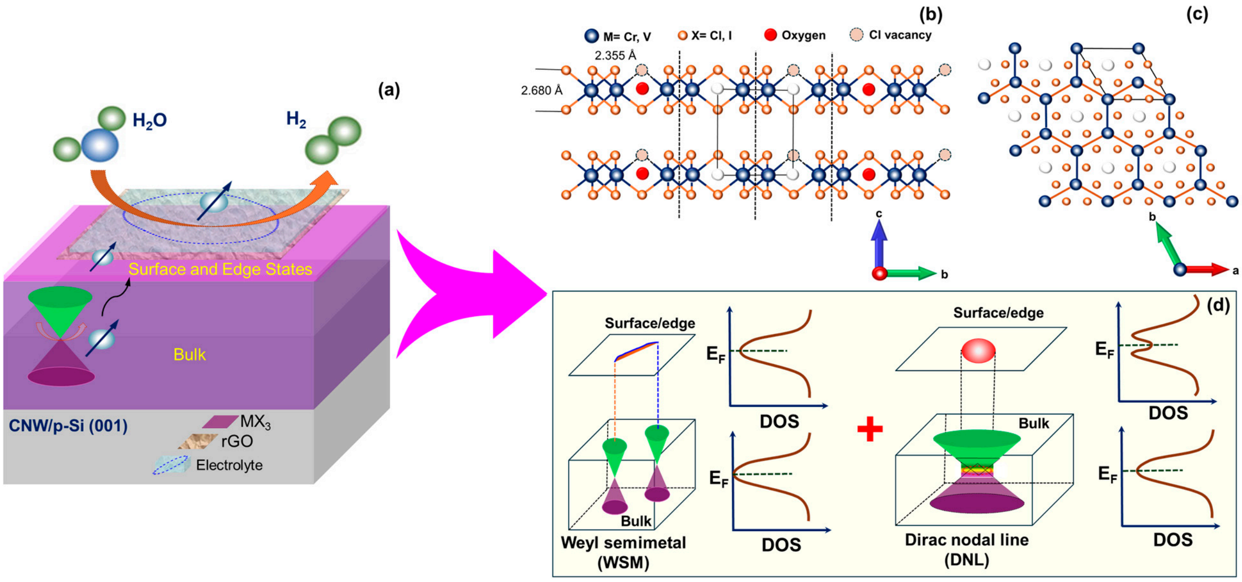

Figure 5. Proposed HER mechanism in relation to the defects and electronic structure. Illustrations of (**a**) the experimental scheme for high efficiency HER (**b**,**c**), the two-dimensional view of the crystal structure for MX_3 viewed along the (**b**) *a*-axis (planar) and (**c**) *c*-axis (side view), where the M (=Cr, V) atoms are the bigger spheres, and the X (Cl, I) atoms are the smaller spheres. The MX_6 octahedra form a layered honeycomb lattice via edge-sharing within each layer, and the layers are stacked in an ABC sequence along the *c*-axis. The bond lengths for $CrCl_3$ are shown in panel (**b**). Also provided are the presence of the Cl vacancy (dotted circle) and the vacant interstitial sites occupied by oxygen (solid red circle) in the honeycomb array responsible for the HER reaction. (**d**) Cartoons of a momentum space diagram and the DOS (density of states) for topological magnetic materials with the coexistence of the WSM and DNL behaviors of the surface/edge states.

3. Methods

Synthesis and characterization of electrocatalysts. High-quality single crystals of the abovementioned layered magnetic materials of 10 mm × 10 mm × sub-mm size were grown via a self-transport technique starting from polycrystalline commercially available precursor powders or from the stoichiometric ratio of the constituent elements (e.g., $CrCl_3$—Alfa-Aesar (Haverhill, MA, USA) 200050, 98% purity; VCl_3—Sigma-Aldrich (St. Louis, MO, USA) 208272 ≥99% purity; V—Alfa-Aesar 262935, 99.5% purity; and iodine (I_2) pieces—Fisher Scientific (Hampton, NH, USA), ≥99.9% purity, for VI_3 and VI_2). Briefly, the polycrystalline powder was first subjected to oxygen purification cycles and then sealed in a 20-cm-long quartz glass tube. The tubes were then placed in a three-zone horizontal furnace in appropriate temperature gradients, with a temperature gradient of 25 °C between the hot and cold zones. The hot end of the tube was heated at 1000 °C, with a 50 °C per hour heating rate, maintained at this temperature for 1 h, and then slowly cooled down to 700 °C, at a 3 °C per hour cooling rate. The quartz tube was then held between 700 °C and 200 °C and kept there for 7–10 days. More details on the growth procedure can be found in refs. [32,34]. The as-grown crystals were obtained in the form of shiny intense purple ($CrCl_3$), blackish (VCl_3 and VI_3), and red–orange (VI_2) flakes, as shown in Figure 1. The crystals were stored and manipulated in a glove box with an Argon (Ar) gas atmosphere to avoid oxidation and water contamination. For evaluating the HER performance, a few layers were mechanically exfoliated from large flakes using the Scotch tape method, as with traditional layered graphene and TMDCs from bulk counterparts on 285 nm SiO_2/p-Si (100) substrates, as well as using an adhesive polydimethylsiloxane (PDMS) film, and cured at 80 °C. Prior to flake transfer, the substrates were cleaned with acetone, methanol, isopropanol, and deionized water for 10 min each in an ultrasonic bath. Interestingly, since these crystals were insulating, and the electrochemical response was weaker, we used nanocarbon coated substrates CNW/p–Si (100) that allowed better conduction without the SiO_2 film. X-ray diffraction (XRD) was performed to determine the structure and orientation of the free-standing crystals using a Bruker D8 diffractometer (Bremen, Germany) with Cu Kα radiation in the 10–100° 2θ range. For these experiments, a crystal plate was laid down on a zero-background holder. The JCPDS card nos. for each of the XRD spectra are provided, according to the current ICDD. Micro-Raman spectroscopy was performed with a Renishaw InVia spectrometer (West Dundee, IL, USA), equipped with an optical microscope model Olympus BXF41 (with 50X objective, Waltham, MA, USA), operated with 514 nm (Ar^+-laser, E_L = 2.14 eV). The Raman spectra were calibrated against the Si peak at 520 cm^{-1}.

Catalytic Performance Tests. The electrochemical measurements were performed using Potentiostat–Galvanostat VMP-300 Bio-Logic (Seyssinet-Pariset, France) and EC-Lab software ver. 11.52 with a custom made three-electrode electrochemical cell in 1M KOH (pH = 13.67) and 0.5 M of H_2SO_4 (pH = 1.3) electrolytes. While linear sweep voltammetry (LSV) profiles were recorded with scan rates of 5 mV/s and 10 mV/s in potential range −0.5 V–+1.6 V (or −0.6 V to +1 V vs. RHE), cyclic voltammetry (CV) curves were recorded with scan rate of 20, 40, 60, 80, 100 mV/s in potential range −0.5 V–+1.5 V (or −0.6 V to +1.0 V vs. RHE) with MX_3 layers as the working electrode, Ag/AgCl as the reference electrode and platinum helical wire as the counter electrode. The chronoamperometric tests were used sparsely to characterize the electrodes' stability. The geometric surface area of the electrode immersed in the electrolyte was A = 0.205 cm^2. All overpotentials referred to RHE (reversible hydrogen electrode) calculated using the following equation: $E_{(RHE)} = E_{(Ag/AgCl)} + E_{o\,(Ag/AgCl)} + 0.059 \times pH$ (V), where E_0(Ag/AgCl) = 0.1976 V. *iR*-compensation due to solution resistance (R_s) was performed that was determined from the electrochemical impedance spectroscopy at 0V (vs. RHE) in frequency range from 200 kHz to 100 mHz with 25 mV AC dither. The Tafel plots recorded with LSV at low overpotentials fitted to the Tafel equation: $\eta = b \log |j| + a$, where η the overpotential ($E - E_0$), j the current density, b the Tafel slope, and $a = \log |j_0|$, the exchange current density.

4. Conclusions

In summary, we report the unprecedented reasonable electrocatalytic activity for hydrogen evolution reaction from few layers of transition metal trihalides as potential quantum electrocatalysts having distinct electronic and magnetic behavior exposing unique surface states in acidic and alkaline solutions while discerning the reaction mechanisms at low and high current densities, which is comparable to those advanced electrocatalysts investigated. Specifically, we determined required overpotentials ranging from 30−50 mV under 10 mA cm^{-2} and 400−510 mV (0.5M H_2SO_4) and 280−500 mV (1M KOH) under 1000 mA cm^{-2} current densities. Likewise, Tafel slopes ranged between 27−36 mV dec^{-1} (Volmer-Tafel) and 110−190 mV dec^{-1} (Volmer–Herovsky) implying the different working mechanisms at low and high current densities, respectively. We attributed this activity at high current densities primarily to unusual synergistic effect between surface chemistry (atomic level defects and subsurface semi oxide) and layered structure influencing catalysis, whereby the layer facilitates a barrier-free water dissociation while the active halogen site (or absence thereof as electroactive defect site) layer promotes favorable hydrogen adsorption and evolution through recombination. These defect-triggered vacancy formation and in-gap states factor into the control and performance parameters desirably. The DFT simulations corroborated the defect associated structure changes and favorable hydrogen evolution reaction analogous to mono- and di-vacancy as well as substitution of sulfur by oxygen in 2H–MoS_2 surfaces. Such behavior is anticipated to be accelerated for systems down to bi-/trilayers while exemplifying the critical role of catalysts with quantum nature and defect sites for industrial-relevant conditions. These experimental findings serve as a bedrock on the potential of quantum electrocatalysts that could withstand harsh conditions of industrial-scale hydrogen production while protected not only by a thin carbon layer, but also topological surface states. The future scope is to improve activity by tuning catalytic reaction pathways for abundant clean energy by employing an unexplored territory of electrochemical-induced activation under external magnetic field.

Supplementary Materials: The following supporting information can be downloaded at: https://www.mdpi.com/article/10.3390/catal14100676/s1, Figures S1 and S2: The impedance spectroscopy and performance comparison with other significant catalysts.

Author Contributions: Conceptualization, S.G.; methodology, S.G. and T.K.; software, S.G. and R.B.; validation, S.G., R.B., H.Ś. and T.K.; formal analysis, S.G. and H.Ś.; investigation, S.G. and H.Ś.; resources, S.G., R.B., M.S. and T.K.; data curation, S.G. and H.Ś.; writing—original draft preparation, S.G.; writing—review and editing, S.G., H.Ś., M.S., T.K. and R.B.; visualization, S.G., H.Ś. and T.K.; supervision, S.G. and R.B.; project administration, S.G.; funding acquisition, S.G. and T.K. All authors have read and agreed to the published version of the manuscript.

Funding: This research received no external funding.

Data Availability Statement: The original contributions presented in the study are included in the article/Supplementary Material, further inquiries can be directed to the corresponding author/s.

Acknowledgments: The author (S.G.) acknowledges the support of these studies from Gdańsk University of Technology by the DEC-37/2022/IDUB/1.1 grant under the NOBELIUM Support for Highly Qualified Scientists Program. The authors are also thankful to the anonymous reviewers for their valuable feedback to the peer review which improved the manuscript.

Conflicts of Interest: The authors declare no conflict of interest.

References

1. Lu, T.N.V.; Barbir, F. Hydrogen: The wonder fuel. *Int. J. Hydrogen Energy* **1992**, *17*, 391–400.
2. Faber, M.S.; Jin, S. Earth-abundant inorganic electrocatalysts and their nanostructures for energy conversion applications. *Energy Environ. Sci.* **2014**, *7*, 3519–3542. [CrossRef]
3. Singh, A.K.; Xu, Q. Synergistic catalysis over bimetallic alloy nanoparticles. *ChemCatChem Catal.* **2013**, *5*, 652–676. [CrossRef]
4. Shiraishi, Y.; Sakamoto, H.; Sugano, Y.; Ichikawa, S.; Hirai, T. Pt–Cu bimetallic alloy nanoparticles supported on anatase TiO_2: Highly active catalysts for aerobic oxidation driven by visible light. *ACS Nano* **2013**, *7*, 9287–9297. [CrossRef] [PubMed]
5. Fujishima, A.; Honda, K. Electrochemical photolysis of water at a semiconductor electrode. *Nature* **1972**, *238*, 37–58. [CrossRef] [PubMed]
6. Stamenkovic, V.R.; Mun, B.S.; Arenz, M.; Mayrhofer, K.J.J.; Lucas, C.A.; Wang, G.; Ross, P.N.; Markovic, N.M. Trends in electrocatalysis on extended and nanoscale Pt-bimetallic alloy surfaces. *Nat. Mater.* **2007**, *6*, 241–247. [CrossRef] [PubMed]
7. Veziroglu, T.N.; Sahin, S. 21st Century's energy: Hydrogen energy system. *Energy Convers. Manag.* **2008**, *49*, 1820–1831. [CrossRef]
8. Kibsgaard, J.; Chen, Z.; Reinecke, B.N.; Jaramillo, T.F. Engineering the surface structure of MoS_2 to preferentially expose active edge sites for electrocatalysis. *Nat. Mater.* **2012**, *11*, 963–969. [CrossRef]
9. Wang, M.; Wang, Z.X.; Gong, X.; Guo, Z. The intensification technologies to water electrolysis for hydrogen production—A review. *Renew. Sustain. Energy Rev.* **2014**, *29*, 573–588. [CrossRef]
10. Chen, H.; Zhou, Y.; Guo, W.; Xia, B.Y. Emerging two-dimensional nanocatalysts for electrocatalytic hydrogen production. *Chin. Chem. Lett.* **2022**, *33*, 1831–1840. [CrossRef]
11. Zhang, L.; Shi, Z.; Lin, Y.; Chong, F.; Qi, Y. Design Strategies for Large Current Density Hydrogen Evolution Reaction. *Front. Chem.* **2022**, *10*, 866415. [CrossRef] [PubMed]
12. Yao, R.; Sun, K.; Zhang, K.; Wu, Y.; Du, Y.; Zhao, Q.; Liu, G.; Chen, C.; Sun, Y.; Li, J. Stable hydrogen evolution reaction at high current densities via designing the Ni single atoms and Ru nanoparticles linked by carbon bridges. *Nat. Commun.* **2024**, *15*, 2218. [CrossRef]
13. Zhao, J.; Urrego-Ortiz, R.; Liao, N.; Calle-Vallejo, F.; Luo, J. Rationally designed Ru catalysts supported on TiN for highly efficient and stable hydrogen evolution in alkaline conditions. *Nat. Commun.* **2024**, *15*, 6391. [CrossRef]
14. Li, D.; Wang, R.; Yi, L.; Wei, Y.; Li, J.; Zhao, D.; Sun, W.; Hu, W. High current density hydrogen evolution on heterostructured Ni/Cr bimetallic sulfide catalyst in alkaline media. *Int. J. Hydrogen Energy* **2024**, *49 Pt C*, 67–74. [CrossRef]
15. Zheng, Z. Boosting hydrogen evolution on MoS_2 via co-confining selenium in surface and cobalt in inner layer. *Nat. Commun.* **2020**, *11*, 3315. [CrossRef] [PubMed]
16. Gupta, S.; Robinson, T.; Dimakis, N. Electrochemically desulfurized molybdenum disulfide (MoS_2) and reduced graphene oxide aerogel composites as efficient electrocatalysts for hydrogen evolution. *J. Nanosci. Nanotechnol.* **2020**, *20*, 6191–6214. [CrossRef]
17. Dimakis, N.; Vadodariab, O.; Ruiz, K.; Gupta, S. Molybdenum disulfide monolayer electronic structure information as explored using density functional theory and quantum theory of atoms in molecules. *Appl. Surf. Sci.* **2021**, *555*, 149545. [CrossRef]

18. Arandiyan, H.; Mofarah, S.S.; Wang, Y.; Cazorla, C.; Jampaiah, D.; Garbrecht, M.; Wilson, K.; Lee, A.F.; Zhao, C.; Maschmeyer, T. Impact of surface defects on $LaNiO_3$ perovskite electrocatalysts for oxygen evolution reaction. *Chem. A Eur. J.* **2021**, *27*, 14418–14426. [CrossRef] [PubMed]
19. Zhang, Y.; Arpino, K.E.; Yang, Q.; Kikugawa, N.; Sokolov, D.A.; Hicks, C.W.; Liu, J.; Felser, C.; Li, G. Observation of a robust and active catalyst for hydrogen evolution under high current densities. *Nat. Commun.* **2022**, *13*, 7784. [CrossRef] [PubMed]
20. Fittipaldi, R.; Hartmann, R.; Mercaldo, M.T.; Komori, S.; Bjørlig, A.; Kyung, W.; Yasui, Y.; Miyoshi, T.; Olthof, L.A.B.O.; Garcia, C.M.P.; et al. Unveiling unconventional magnetism at the surface of Sr_2RuO_4. *Nat. Commun.* **2021**, *12*, 5792. [CrossRef] [PubMed]
21. Zhu, Y.; Tahini, H.A.; Hu, Z.; Dai, J.; Chen, Y.; Sun, H.; Zhou, W.; Liu, M.; Smith, S.C.; Wang, H.; et al. Unusual synergistic effect in layered Ruddlesden–Popper oxide enables ultrafast hydrogen evolution. *Nat. Commun.* **2019**, *10*, 149. [CrossRef]
22. Luo, H.; Yu, P.; Li, G.; Yan, K. Topological quantum materials for energy conversion and storage. *Nat. Rev. Phys.* **2022**, *4*, 611–624. [CrossRef]
23. Yan, B.; Felser, C. Topological Materials: Weyl Semimetals. *Annu. Rev. Condens. Matter Phys.* **2017**, *8*, 337–354. [CrossRef]
24. Xiao, J.; Kou, L.; Yam, C.-Y.; Fraunheim, T.; Yan, B. Toward Rational Design of Catalysts Supported on a Topological Insulator Substrate. *ACS Catal.* **2015**, *5*, 7063–7067. [CrossRef]
25. Rajamathi, C.R.; Gupta, U.; Pal, K.; Kumar, N.; Yang, H.; Sun, Y.; Shekar, C.; Yan, B.; Parkin, S.S.P.; Waghmare, U.V.; et al. Photochemical Water Splitting by Bismuth Chalcogenide Topological Insulators. *ChemPhysChem* **2017**, *18*, 2322–2327. [CrossRef]
26. Zhang, X.; Wang, L.; Li, M.; Meng, W.; Liu, Y.; Dai, X.; Liu, G.; Gu, Y.; Liu, J.; Kou, L. Topological surface state: Universal catalytic descriptor in topological catalysis. *Mater. Today* **2023**, *67*, 23–32. [CrossRef]
27. Yu, X.; Cao, X.; Kang, W.; Chen, S.; Jiang, A.; Luo, Y.; Deng, W. Efficient hydrogen production over Bi_2Te_3-modified TiO_2 catalysts: A first principles study. *Surf. Sci.* **2024**, *739*, 122401. [CrossRef]
28. Sakaushi, K. Quantum electrocatalysts: Theoretical picture, electrochemical kinetic isotope effect analysis, and conjecture to understand microscopic mechanisms. *Phys. Chem. Chem. Phys.* **2020**, *22*, 11219–11243. [CrossRef] [PubMed]
29. Kim, H.H.; Yang, B.; Li, S.; Jiang, S.; Jin, C.; Tao, Z.; Nichols, G.; Sfgakis, F.; Zhong, S.; Li, C.; et al. Evolution of interlayer and intralayer magnetism in three atomically thin chromium trihalides. *Proc. Natl. Acad. Sci. USA* **2019**, *166*, 11131–11136. [CrossRef]
30. Wang, Z.; Gutiérrez-Lezama, I.; Ubrig, N.; Kroner, M.; Gibertini, M.; Taniguchi, T.; Watanabe, K.; Imamoglu, A.; Giannini, E.; Morpurgo, A.F. Very large tunneling magnetoresistance in layered magnetic semiconductor CrI_3. *Nat. Commun.* **2018**, *9*, 2516. [CrossRef]
31. Huang, B.; Clark, G.; Navarro-Moratalla, E.; Klein, D.R.; Cheng, R.; Seyler, K.L.; Zhong, D.; Schmidgall, E.; McGuire, M.A.; Cobden, D.H.; et al. Layer-dependent ferromagnetism in a van der Waals crystal down to the monolayer limit. *Nature* **2017**, *546*, 270–273. [CrossRef]
32. Mastrippolito, D.; Ottaviano, L.; Wang, J.; Yang, J.; Gao, F.; Ali, M.; D'Olimpio, G.; Politano, A.; Palleschi, S.; Kazim, S.; et al. Emerging oxidized and defective phases in low-dimensional $CrCl_3$. *Nanoscale Adv.* **2021**, *3*, 4756–4766. [CrossRef]
33. Kazim, S.; Mastrippolito, D.; Moras, P.; Jugovac, M.; Klimczuk, T.; Ali, M.; Ottaviano, L.; Gunnella, R. Synchrotron radiation photoemission spectroscopy of the oxygen modified $CrCl_3$ surface. *Phys. Chem. Chem. Phys.* **2023**, *25*, 3806–3814. [CrossRef]
34. Kazim, S.; Ali, M.; Palleschi, S.; D'Olimpio, G.; Mastrippolito, D.; Politano, A.; Gunnella, R.; Di Cicco, A.; Renzelli, M.; Moccia, G.; et al. Mechanical Exfoliation and Layer Number Identification of Single Crystal Monoclinic $CrCl_3$. *Nanotechnology* **2020**, *31*, 395706. [CrossRef]
35. Zhang, Y.; Wang, L.; Chen, Q.; Cao, J.; Zhang, C. Recent progress of electrochemical hydrogen evolution over 1T-MoS_2 catalysts. *Front. Chem.* **2022**, *10*, 1000406. [CrossRef] [PubMed]
36. Zhang, W.; Liao, X.; Pan, X.; Yan, M.; Li, Y.; Tian, X.; Zhao, Y.; Xu, L.; Mai, L. Superior Hydrogen Evolution Reaction Performance in 2H-MoS_2 to that of 1T Phase. *Small* **2019**, *15*, 1900964. [CrossRef] [PubMed]
37. Sharma, L.; Botari, T.; Tiwary, C.S.; Halder, A. Hydrogen Evolution at the In Situ MoO_3/MoS_2 Heterojunctions Created by Nonthermal O_2 Plasma Treatment. *ACS Appl. Energy Mater.* **2020**, *3*, 5333–5342. [CrossRef]
38. Sobaszek, M.; Siuzdak, K.; Ryl, J.; Sawczak, M.; Gupta, S.; Carrizosa, S.B.; Ficek, M.; Dec, B.; Darowicki, K.; Bogdanowicz, R. Diamond phase (sp^3–C) rich boron-doped carbon nanowalls (sp^2–C): Physicochemical and electrochemical properties. *J. Phys. Chem. C* **2017**, *121*, 20821–20833. [CrossRef]
39. Paolucci, V.; Mastrippolito, D.; Ricci, V.; Świątek, H.; Klimczuk, T.; Ottaviano, L.; Cantalini, C. Two-Dimensional $CrCl_3$-Layered Trihalide Nanoflake Sensor for the Detection of Humidity, NO_2, and H_2. *ACS Appl. Nano Mater.* **2024**, *7*, 3679–3690. [CrossRef]
40. Wang, Z.; Gibertini, M.; Dumcenco, D.; Taniguchi, T.; Watanabe, K.; Giannini, E.; Marpurgo, A.F. Determining the phase diagram of atomically thin layered antiferromagnet $CrCl_3$. *Nat. Nanotechnol.* **2019**, *14*, 1116–1122. [CrossRef]
41. Morosin, B.; Narath, A. X-ray Diffraction and Nuclear Quadrupole Resonance Studies of Chromium Trichloride. *J. Chem. Phys.* **1964**, *40*, 1958–1967. [CrossRef]
42. Tian, S.; Zhang, J.-F.; Li, C.; Ying, T.; Li, S.; Zhang, X.; Liu, K.; Lei, H. Ferromagnetic van der Waals Crystal VI_3. *J. Am. Chem. Soc.* **2019**, *141*, 5326–5333. [CrossRef]
43. Munro, J.M.; Latimer, K.; Horton, M.K.; Dwaraknath, S.; Persson, K.A. An improved symmetry-based approach to reciprocal space path selection in band structure calculations. *Npj Comput. Mater.* **2020**, *6*, 112. [CrossRef]
44. Mastrippolito, D.; Camerano, L.; Świątek, H.; Šmíd, B.; Klimczuk, T.; Ottaviano, L.; Profeta, G. Polaronic and Mott insulating phase of layered magnetic vanadium trihalide VCl_3. *Phys. Rev. B* **2023**, *108*, 045126. [CrossRef]

45. Glamazda, A.; Lemmens, P.; Do, S.H.; Kwon, S.Y.; Choi, K.Y. Relation between Kitaev magnetism and structure in α–$RuCl_3$. *Phys. Rev. B* **2017**, *95*, 174429. [CrossRef]
46. Avram, C.; Gruia, A.; Brik, M.; Barb, A. Calculations of the electronic levels, spin-hamiltonian parameters and vibrational spectra for the $CrCl_3$ layered crystals. *Phys. B Condens. Matter* **2015**, *478*, 31–35. [CrossRef]
47. Kong, T.; Stolze, K.; Timmons, E.I.; Tao, J.; Ni, D.; Guo, S.; Yang, Z.; Prozorov, R.; Cava, R.J. Ferromagnetic Semiconductors: VI_3–a New Layered Ferromagnetic Semiconductor. *Adv. Mater.* **2019**, *31*, 1970126. [CrossRef]
48. Suhan, S.; Matthew, J.C.; Nahyun, L.; Jonghyeon, K.; Yun, K.T.; Hayrullo, H.; Hwanbeom, C.; Cheng, L.; David, M.J.; Philip, A.C.B.; et al. Bulk properties of the van der Waals hard ferromagnet VI_3. *Phys. Rev. B* **2019**, *99*, 041402.
49. He, B.-G.; Yang, Z.; Cheng, Z.-P.; Zhang, W.-B.; Li, H. Raman Spectrum of layered Ferromagnetic Material VI_3 from First-principles. In Proceedings of the 9th IEEE International Symposium on Next-Generation Electronics, Changsha, China, 10–12 July 2021. [CrossRef]
50. Hong, M.; Dai, L.; Hu, H.; Zhang, X.; Li, C.; He, Y. Pressure-Induced Structural Phase Transition and Metallization of $CrCl_3$ under Different Hydrostatic Environments up to 50.0 GPa. *Inorg. Chem.* **2022**, *61*, 4852–4864. [CrossRef] [PubMed]
51. Harrington, D.A.; Conway, B.E. ac Impedance of Faradaic reactions involving electrosorbed intermediates—I. Kinetic theory. *Electrochim. Acta* **1987**, *32*, 1703–1712. [CrossRef]
52. Krstajić, N.; Popović, M.; Grgur, B.; Vojnović, M.; Šepa, D. On the kinetics of the hydrogen evolution reaction on nickel in alkaline solution: Part I. *Mech. J. Electroanal. Chem.* **2001**, *512*, 16–26. [CrossRef]
53. Zheng, Y.; Jiao, Y.; Jaroniec, M.; Qiao, S.Z. Advancing the Electrochemistry of the Hydrogen-Evolution Reaction through Combining Experiment and Theory. *Angew. Chem. Int. Ed.* **2015**, *54*, 52–65. [CrossRef]
54. Tian, X.; Zhao, P.; Sheng, W. Hydrogen Evolution and Oxidation: Mechanistic Studies and Material Advances. *Adv. Mater.* **2019**, *31*, 1808066. [CrossRef]
55. de Chialvo, M.R.G.; Chialvo, A.C. Existence of two sets of kinetic parameters in the correlation of the hydrogen electrode reaction. *J. Electrochem. Soc.* **2000**, *147*, 1619–1622. [CrossRef]
56. Durst, J.; Siebel, A.; Simon, C.; Hasché, F.; Herranz, J.; Gasteiger, H.A. New insights into the electrochemical hydrogen oxidation and evolution reaction mechanism. *Energy Environ. Sci.* **2014**, *7*, 2255–2260. [CrossRef]
57. Vliekar, S.A.; Fishtik, I.; Datta, R. Kinetics of the hydrogen electrode reaction. *J. Electrochem. Soc.* **2010**, *157*, B1040–B1050. [CrossRef]
58. Parsons, R. The rate of electrolytic hydrogen evolution and the heat of adsorption of hydrogen. *Trans. Farad. Soc.* **1958**, *54*, 1053–1063. [CrossRef]
59. Li, G.; Fu, C.; Shi, W.; Jiao, L.; Wu, J.; Yang, Q.; Saha, R.; Kamminga, M.E.; Srivastava, A.K.; Liu, E.; et al. Dirac nodal arc semimetal $PtSn_4$: An ideal platform for understanding surface properties and catalysis for hydrogen evolution. *Angew. Chem. Int. Ed.* **2019**, *58*, 13107–13112. [CrossRef] [PubMed]
60. Bezanilla, A.L. Interplay between p$-$ and d$-$ orbitals yields multiple Dirac states in one- and two-dimensional CrB_4. *2D Mater.* **2018**, *5*, 035041. [CrossRef]